

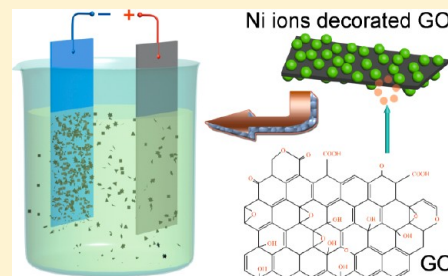
One-Step Electrophoretic Deposition of Reduced Graphene Oxide and Ni(OH)₂ Composite Films for Controlled Syntheses Supercapacitor Electrodes

Haitao Zhang, Xiong Zhang, Dacheng Zhang, Xianzhong Sun, He Lin, Changhui Wang, and Yanwei Ma*

Institute of Electrical Engineering, Chinese Academy of Sciences, Beijing 100190, People's Republic of China

S Supporting Information

ABSTRACT: A facile, rapid, scalable, and environmentally friendly electrophoretic deposition (EPD) approach has been developed for the fabrication of reduced graphene oxide (RGO) and Ni(OH)₂ syntheses based on EPD of graphene oxide (GO) and Ni(NO₃)₂ colloidal suspension. Nickel ion decoration made GO positively charged and further made cathodic EPD feasible. Direct assembly by one-step EPD facilitated transformation from GO to RGO and resulted in multilayer or flower-like RGO/Ni(OH)₂ hybrid films on different substrates. X-ray diffraction analysis suggested that the crystal structures of Ni(OH)₂ depended on the colloidal suspension and the substrate. Further transmission electron microscopy characterization indicated that Ni(OH)₂ nanoclusters composed of 5–10 nm nanoparticles in grain size were homogeneously dispersed and anchored on the RGO. The resulting 100% binder-free RGO/Ni(OH)₂ electrodes exhibited excellent pseudocapacitive behavior with high specific capacitance of 1404 F g⁻¹ at 2 A g⁻¹, high rate capability, and good electrochemical cyclic stability. These results paved the way for EPD to produce RGO-based nanocomposite films for high-performance energy storage devices.



INTRODUCTION

Supercapacitors, also called electrochemical capacitors or ultracapacitors, are considered one of the most important types of devices for next-generation energy storage due to their high power densities and excellent cycling stability.^{1–3} Research into supercapacitors is presently divided into two main areas that are based primarily on their mechanism of energy storage, i.e., an electrostatic attraction as in electrical double layer capacitors (EDLCs) and pseudocapacitors originated from quick faradaic charge transfer reactions similar to processes proceeding in batteries.⁴ The most commonly investigated classes of EDLCs materials are carbon materials, which store energy by means of charge separation and exhibit a very high degree of reversibility in repetitive charge–discharge cycling life in excess of 500 000 cycles.⁵ However, the specific capacitance of carbon materials is low in EDLCs due to the limited accessibility of the carbon surface to electrolyte.⁶ Fortunately, the specific capacitance of some transition metal oxides or hydroxide-based pseudocapacitive materials such as RuO₂, MnO₂, Ni(OH)₂, and cobalt nickel layered double hydroxides,^{7–10} the same as in Conway et al. calculation, can be 10–100 times higher than EDLCs,¹¹ which significantly enhance the energy density of supercapacitors. However, it usually suffers from relatively lower power density and lacks stability during cycling.¹² Thus, the development of carbon and transition metal oxide or hydroxide composite materials may mediate the paradox of two kinds of supercapacitors and overcome the major challenges posed by the low energy density and relatively high cost of supercapacitors.

Electrophoretic deposition (EPD) is a colloidal process wherein materials are shaped directly from a stable suspension under an applied electric field. Interest in the EPD technique is driven not only by the high versatility of its use with various materials (and combinations) but also by its simplicity and cost-effectiveness requiring simple apparatus.¹³ Although EPD has received great attention in the field of advanced ceramics since the 1980s, and some reasonable mechanisms including particle charge neutralization, electrochemical particle coagulation, electrical double layer distortion, and thinning mechanisms have been introduced for the sake of explaining the process of EPD,¹⁴ the mechanism of EPD is still not completely clear. However, it does not hinder the success of EPD in many fields including coatings, nanoscale assembly, micropatterned thin films, near shape ceramics and glasses, solid oxide fuel cells, laminated or graded materials, hybrid materials, fiber reinforced ceramic matrix composites, and so on.¹⁵ Moreover, EPD, in contrast to other processing methods, offers advantages of low cost, process simplicity, uniformity of deposits, good control of deposit thickness, microstructural homogeneity, and deposition on complex shaped substrates, including the potential to infiltrate porous substrates.¹⁶ All these advantages can also be exploited for forming films and

Special Issue: Electrophoretic Deposition

Received: May 29, 2012

Revised: September 10, 2012

Published: September 20, 2012

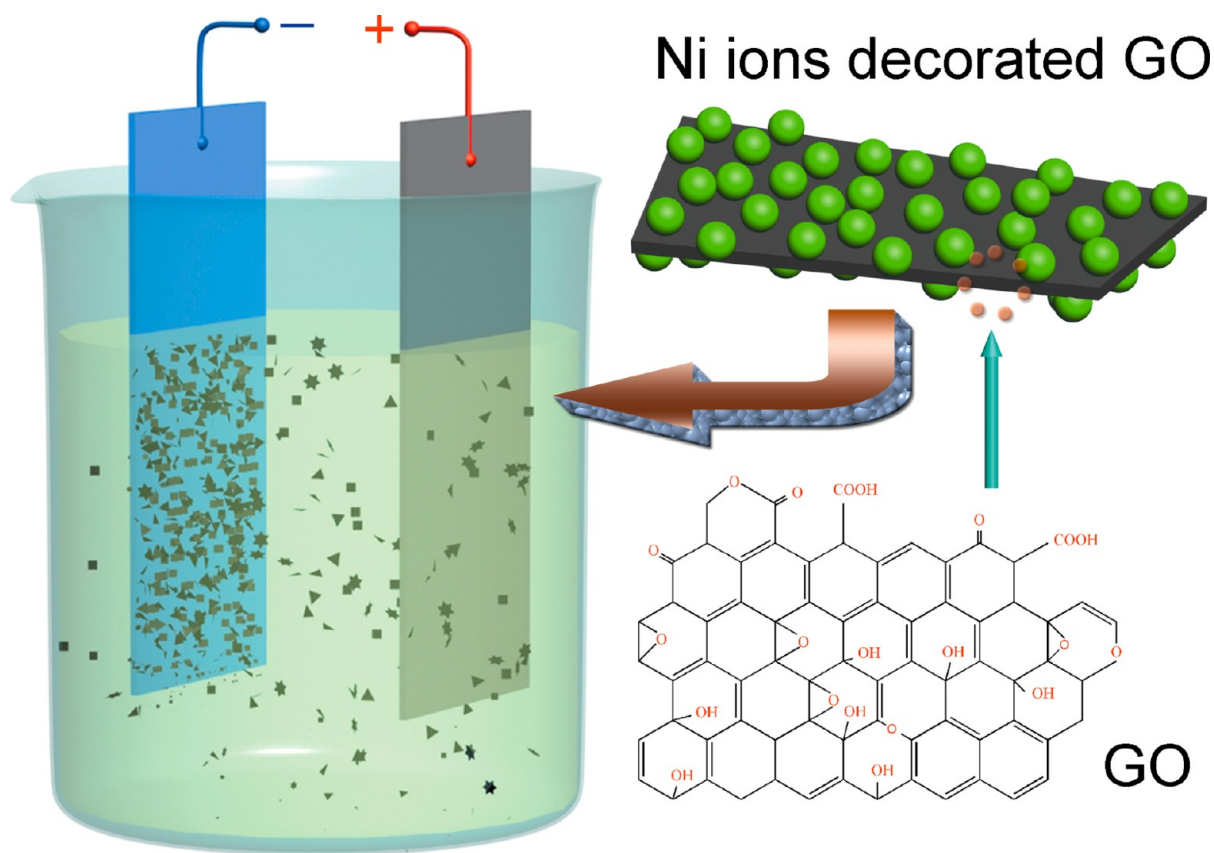


Figure 1. Schematic diagram of EPD.

coatings of graphene oxide (GO)-based or reduced graphene oxide (RGO)-based electrode materials for supercapacitors.

As reported in the literature, Wu et al. pioneered the EPD process of graphene films by analogy to EPD of carbon nanotubes, in which $\text{Mg}(\text{NO}_3)_2$ equaling graphene in weight was added into graphene solution that, when charged by Mg^{2+} ion, would deposit on a cathode electrode under applied voltage at 100–160 V.¹⁷ However, charge or further chemical decoration is not always necessary if graphene or GO itself can form a stable colloidal solution in a suitable solvent. Our group reported that *p*-phenylene diamine RGO homogeneously deposited on indium tin oxide (ITO) substrate, and the conductivity in the plane of the film was 150 S cm^{-1} . These nitrogen ion-functionalized graphene monolayers showed potential application in electrochemical energy storage when deposited on nickel foam (NF) with a three-dimensional (3D) porous structure.^{18,19} Uniform, thickness adjustable and, more importantly, agglomeration-free graphene films were obtained by controlled EPD of hydrazine or KOH modified GO, which was electrostatically stabilized in deionized water solution.²⁰ In addition to being useful to pure graphene or GO, the EPD technique combined with other deposition methods succeeded in preparing some syntheses such as graphene/Pt nanoparticles, graphene/carbon nanotubes, graphene/NiO, graphene/poly-(pyrrole), ternary composites of graphene/porphyrin/ZnO nanoparticles, and so forth.^{21–26}

However, to date, there is no report about the preparation of RGO and $\text{Ni}(\text{OH})_2$ composite films by a one-step EPD process. We have, therefore, sought to use EPD to produce novel RGO/ $\text{Ni}(\text{OH})_2$ electrodes with enhanced electrochemical properties, such as achieving a high specific

capacitance and an increase in $\text{Ni}(\text{OH})_2$ electrochemically cycled lifetime. In this report, we describe a facile, low-cost, scalable method for the development of a new class of binder-free composite materials based on $\text{Ni}(\text{OH})_2$ nanoparticles and RGO platelets. The synthesis is prepared following the procedure shown in Figure 1, which is simply a one-step EPD of $\text{Ni}(\text{NO}_3)_2$ and GO colloidal suspensions on several conductive substrates.

EXPERIMENTAL SECTION

Preparation of GO. GO was synthesized from natural graphite by the modified Hummers method. H_2SO_4 (46 mL) was added into a 500 mL flask filled with graphite (1 g) and NaNO_3 (1 g) at room temperature. The flask was then cooled to 0°C in an ice bath and agitated continuously for 4 h, followed by slow addition of KMnO_4 (6 g) and allowed to warm to room temperature. Next, the mixture was stirred mildly for 2 h before 92 mL of deionized water was carefully added into it. After that, the mixture was moved into a water-bath of 98°C and agitated for 15 min, followed by addition of 200 mL deionized water. Finally, sufficient H_2O_2 was added prior to centrifugation and desiccation.

EPD of RGO/ $\text{Ni}(\text{OH})_2$ Composite Films. In the EPD process, several conductive substrates, including NF, ITO, stainless steel (SS) and platinum (Pt) were the negative electrode. The substrates were rinsed by ultrasonic vibrations in acetone, ethanol, and deionized water, respectively. The positive counter electrode was Pt with the same dimension. Prior to EPD, the GO and $\text{Ni}(\text{NO}_3)_2$ in 50 mL of deionized water were ultrasonically dispersed for 2 h. The electrodes were spaced 10 mm apart and immersed in the colloidal solution

Table 1. The Concrete Parameters of EPD^a

sample	GO/mg	Ni(NO ₃) ₂ /mg	voltage/V	time/s	pH	substrates
GO-1	20		10	60	2.62	NF
GO-2	20		5	60		NF/ITO
GO-3	50		10	60		NF
C1-1	20	5	10	60	2.58	NF
C1-2	20	10	10	60	2.56	NF
C1-3	20	20	10	60	2.46	NF
C1-4	20	146	10	60	2.23	NF
C2-1	20	20	2	120	2.46	NF
C2-2	20	20	5	120		NF
C2-3	20	20	10	120		NF
C3-1	20	20	5	30	2.46	NF
C3-2	20	20	5	60		NF/ITO
C3-3	20	20	5	120		NF/ITO/SS
C3-4	20	20	5	300		NF/ITO/Pt
C3-5	20	20	5	600		NF/ITO
C4-1	20	20	5	60	3.07	NF
C4-2	20	20	5	60	3.64	NF
C4-3	20	20	5	60	4.61	NF
C4-4	20	20	5	60	6.12	NF
C4-5	20	20	5	60	10.73	NF
C4-6	20	20	5	60	11.13	NF

^aNote: The deposited solutions were diluted 10 times to measure the pH value of the samples from C4-1 to C4-6.

Table 2. Mass (mg) of the Samples Deposited on NF Substrate with an Area of 1.5 cm × 1 cm

GO-2	GO-3	C1-1	C1-2	C1-3	C1-4	C2-1	C2-2	C3-1	C3-2	C3-4	C3-5
0.08	1.08	0.10	0.19	0.38	2.21	0.12	0.20	0.11	0.13	0.33	0.37

saturated with nitrogen gas. An applied potential of 2–10 V was used for 30–600 s to deposit. EPD was carried out on an Arbin MSTAT4 multichannel galvanostat/potentiostat instrument with an upper limit voltage of 5 V when applied voltage varied from 2 to 5 V, and on a 3646A array DC voltage source with current accuracy of 10 mA when applied voltage came to 10 V. The concrete parameters are summarized in Table 1. After EPD, the nanocomposite film was dried in an oven at 80 °C overnight. The weight of the samples, shown in Table 2, was measured by a microbalance with an accuracy of 0.01 mg.

Characterization. Field-emission scanning electron microscopy (FESEM) was carried out on Zeiss Sigma scanning electron microscopes. Energy disperse spectroscopy (EDS) was carried out on a EDAX TEAM EDS. Transmission electron microscopy (TEM) and high-resolution transmission electron microscopy (HRTEM) were carried out on a JEOL JSM 2010 transmission electron microscope. The crystal structure of the samples was determined by selected area electron diffraction (SAED). X-ray diffraction (XRD) was carried out on a Rigaku D/max-2500 instrument. X-ray photoelectron spectroscopy (XPS) spectra were recorded on a PHI Quantar SXM (ULVAC-PH INC) instrument. Raman spectra were obtained on a RM 2000 microscopic confocal Raman spectrometer employing a 514 nm laser beam. ζ -Potential was measured by Malvern Nano-ZS MPT-2.

Electrochemical Measurement. Cyclic voltammetry and chronopotentiometry were carried out on a CHI 660C electrochemistry workstation. Cycle-life test was measured on an Arbin MSTAT4 multichannel galvanostat/potentiostat instrument. A three electrode system was used. RGO/Ni(OH)₂ deposited onto NF substrate with an area of 1.5 cm × 1 cm was used as the working electrode. Hg/HgO electrode filled with 1

M NaOH was used as the reference electrode. Platinum sheet with an area of 2.5 cm × 2 cm immersed into the electrolyte was used as a counter electrode. A 6 M aqueous solution of KOH was used as electrolyte, especially, saturated with nitrogen gas for the cyclic-life test. Specific capacitance (S_c) was calculated from the second galvanostatic discharge process, using the following equation:

$$S_c = I\Delta t/m\Delta V \quad (1)$$

where I is charge or discharge current, Δt is the time for a full discharge, m indicates the mass of the active material, and ΔV represents the voltage change after a full discharge.

RESULTS AND DISCUSSION

There are many factors that influence the EPD process such as particle size, the conductivity and ζ -potential of suspension, applied potential and deposition time, and so on. However, if the solvent, the colloidal suspension, and the apparatus of EPD are fixed (in this work, we chose deionized water as solvent and L was constant at 10 mm), according to Ishihara theory,²⁷ in which the deposition weights have been written as follows:

$$W = \frac{2}{3} C \cdot \epsilon_0 \cdot \epsilon_r \cdot \zeta \cdot \left(\frac{1}{\eta} \right) \cdot \left(\frac{E}{L} \right) \cdot t \quad (2)$$

where C is the concentration of the particle, ϵ_0 is the permittivity of vacuum, ϵ_r is the relative permittivity of the solvent, ζ is the ζ -potential of the particles, η is the viscosity of the solvent, E is the applied potential, L is the distance between the electrodes, and t is the deposition time. The EPD process will only be susceptible to the concentration of particles, the applied potential, and the deposition time. Therefore, these three factors are discussed, and the results are shown in Figure

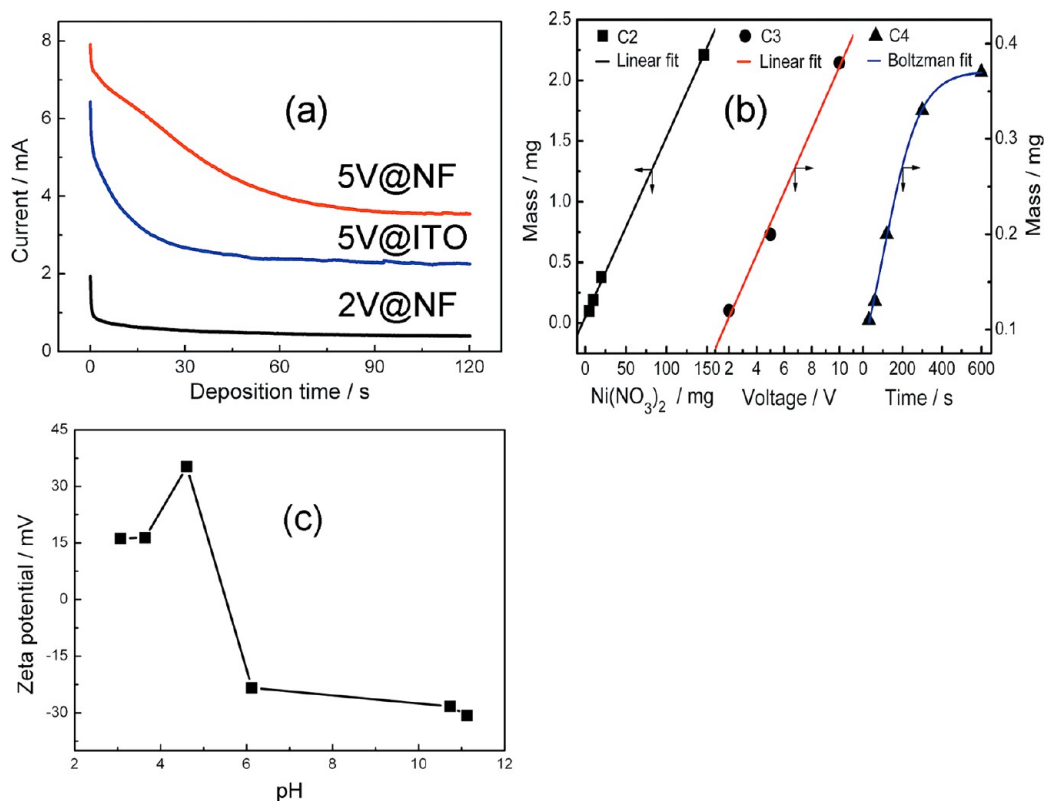


Figure 2. The deposition current and deposition mass of the samples: (a) the current varies with the deposition time; (b) the deposition mass of the materials with different concentration of $\text{Ni}(\text{NO}_3)_2$ additions, deposition voltage and deposition time; (c) ζ -potential of $\text{GO}/\text{Ni}(\text{NO}_3)_2$ as a function of pH, in aqueous solution at a concentration of 0.04 mg mL^{-1} .

2. In spite of deionized water is used as solvate, there is no apparent fluctuation for the deposition current curves varying with the deposition time at different applied potential and substrates (see Figure 2a), which means that the splitting water process is effectively inhibited. In fact, we noticed that there was no evident gas bubble in cathode nearby. Nevertheless, the situation is rather different when the applied potential reaches up to 10 V. Unfortunately, we could not record the deposition current curves because the current accuracy limited to 10 mA of 3646A array EPD apparatus.

The samples reveal the similar mutative tendency of the deposition current curves with three obvious stages, although deposited on different substrates and at different applied potential. The current decreases sharply from 6.43 to 5.58 mA in only 0.21 s (see “blue curve” of Figure 2a). One of the characteristics of the colloidal particles is that they are charged in suspensions. The particles will neutralize their charge as they touch the electrode or deposit.²⁸ Thus, the particle-electrode processes leads to sharp decline phenomenon of the deposition current at the initial stage. With prolonging the deposition time, the deposition current decreases gradually from 5.47 to 2.49 mA in 46 s (also see “blue curve”). The deposition current keeps constant when EPD process executes continuously. However, the reduction of deposition current at the initial stage and the value of constant current at stable stage are related to the applied potential and the substrate.

By adjusting EPD parameters, a series of samples weighing from 0.08 to 2.21 mg on NF substrates were obtained. The deposition mass on the dependence of the concentration of $\text{Ni}(\text{NO}_3)_2$ addition, the deposition voltage and the deposition time is illustrated in Figure 2b. When 20 mg GO is dispersed in

50 mL deionized water, the deposition mass increases linearly with increasing $\text{Ni}(\text{NO}_3)_2$ addition from 5 to 146 mg as does applied potential varying from 2 to 10 V. Apparently, $\text{Ni}(\text{NO}_3)_2$ additions change the pH value of GO, in this work, the pH value is 2.62, 2.58, 2.56, 2.46, and 2.23 (measured at 27 °C) for pure GO and 5–146 mg $\text{Ni}(\text{NO}_3)_2/\text{GO}$ composite aqueous solution, respectively. Note that a high concentration of $\text{Ni}(\text{NO}_3)_2$ addition affects the pH value of GO, and that value is related to the ζ -potential, which is a critical factor to EPD technology. Taking into account the stability of the colloidal suspension, which stabilized for only several hours if the content of 20 mg $\text{Ni}(\text{NO}_3)_2$ was added into the GO suspension, a much higher concentration of $\text{Ni}(\text{NO}_3)_2$ addition than that value was unsuitable for the EPD process.¹⁶ After adding 20 mg $\text{Ni}(\text{NO}_3)_2$ to the stably dispersed GO suspension for charging GO and forming a mixed colloidal solution, the EPD weight of the samples varying from the deposition time was consistent with Lorentz fitting (for detailed results, see Figure S1, Supporting Information). The deposition weight increases fiercely during the initial 30 s and obeys an approximately linear increment from 30 to 300 s, while it increases quite slowly during the following 300 s. The variable tendency can be explained by combining the deposition current curve with the deposition mechanism. It is much easier for the charged particles to achieve the electrode and deposit at the initial stage under an applied potential as long as the potential is strong enough to overcome the repulsion force of particles induced by electrostatic field. The particles attached or deposited on the electrode have the ability to undergo lateral motion because of the lateral attraction between particles, which probably relates to an ionic current through the

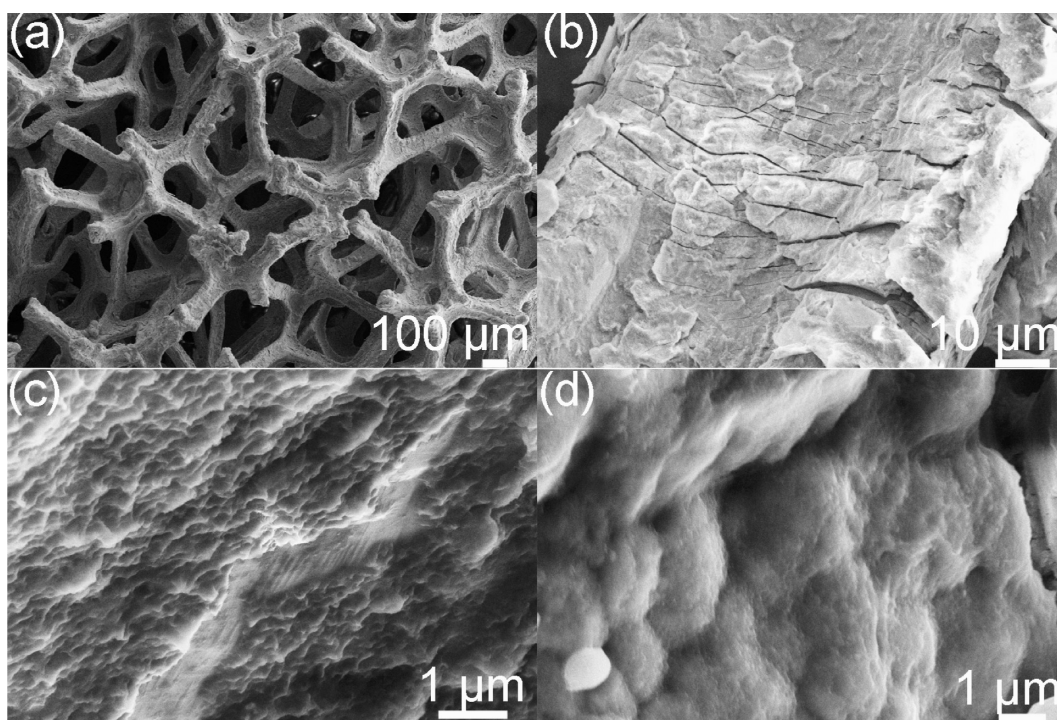


Figure 3. FESEM surface images of the samples deposited on NF substrates: (a) 3D porous structure of NF; (b) GO thick films prepared at a voltage of 10 V and deposition time of 60 s; (c) RGO/Ni(OH)₂ layered porous structure prepared at a voltage of 5 V and deposition time of 60 s; (d) RGO/Ni(OH)₂ sponge-like film prepared at a voltage of 10 V and deposition time of 60 s.

solution.²⁹ Accordingly, a uniform single layer of particles covers the electrode surface, causing somewhat of a decline in the conductivity. The subsequent particles reaching the electrode may originate from different mechanisms such as particle coagulation or particle accumulation mechanisms,³⁰ leading to the gradual decline of deposition current and accompanying the slow increment of the deposition weight. However, the third stage of the much more slower increment with the deposition time from 300 to 600 s is mainly attributed to the water splitting process, which causes failure to deposit uniformly thick films. It was supported that the film, especially on ITO substrates, lost its homogeneity by naked-eye observation. In short, we produced a series of RGO/Ni(OH)₂ film composites weighing 0.08–2.21 mg on different conductive substrates by one-step EPD technology under a rather low applied voltage.

For further discussing the influence of pH on the deposition process, we adjusted the pH value by adding controlled 1 M KOH aqueous solution on the basis of 0.4 g L⁻¹ GO/Ni(NO₃)₂ solution. The solution was diluted 10 times to measure ζ -potential. The ζ -potential of the deposited solution as a function of pH is shown in Figure 2c. The ζ -potential is positive due to Ni ion-decorated GO when the pH is lower than a value of 5, that is, the solutions do not add or add few KOH. However, Ni ions can not effectively interact with GO platelets when much more KOH is added to the deposited solution, in which the pH value is higher than a value of 6. The high negative ζ -potential is the characteristic of GO due to ionization of the carboxylic acid and phenolic hydroxyl groups that are known to exist on the GO platelets.³³ By the way, we also measured a negative ζ -potential of the solution with the pH value lower than a value of 5, which means that Ni ions can not completely decorate GO platelets.

Figure 3 shows FESEM surface images of the samples deposited on NF substrates. The 3D porous structure of NF is shown in Figure 3a. We chose NF as the deposited substrate because of its special 3D network porous structure that is not only good for EPD, as a porous structure has been proved to efficiently absorb the gas bubble, if any, but also it seems like an appropriate current collector for supercapacitors application.³¹ Pure GO colloidal was directly deposited on the NF substrate by the anodic EPD process. The GO thick film displayed in Figure 3b has a massive structure and loses its uniformity. Moreover, there are many cracks present in the films, demonstrating that the binding force between GO and NF substrate is not enough on one hand; on the other hand, gas bubbles resulting from water decomposition of EPD under an applied potential of 10 V probably induce the crack of pure GO films. As metal ions are incorporated into the carbon materials, the cohesion between carbon materials and the substrate was greatly improved.³² Here in this work, the EPD of mixed GO and Ni(NO₃)₂ suspensions yields the crack-free films shown in Figure 3c. The presence of carbon, oxygen, and nickel atoms was confirmed by EDS characterization (see Figure S2). Nickel ions decorated the GO deposits on the electrode under an applied potential, and, simultaneously, nickel ions transform into Ni(OH)₂ through the EPD process. Furthermore, nickel ions can adsorb or chemically interact with layered GO functionalized by oxygen functional groups such as hydroxyls, epoxides, carboxyls, and so on.^{33,34} That interaction results in agglomeration-free RGO-based composites and therefore forms a perfect multilayer structure, just like that illustrated in Figure 3c. The multilayer structure also succeeded in graphene and polyaniline composites, including polyaniline nanowires and nanofibers.^{35–37} However, the multilayer structure changes into the sponge-like structure displayed in Figure 3d when a higher deposition voltage of 10 V is used. Surprisingly, the sponge-like

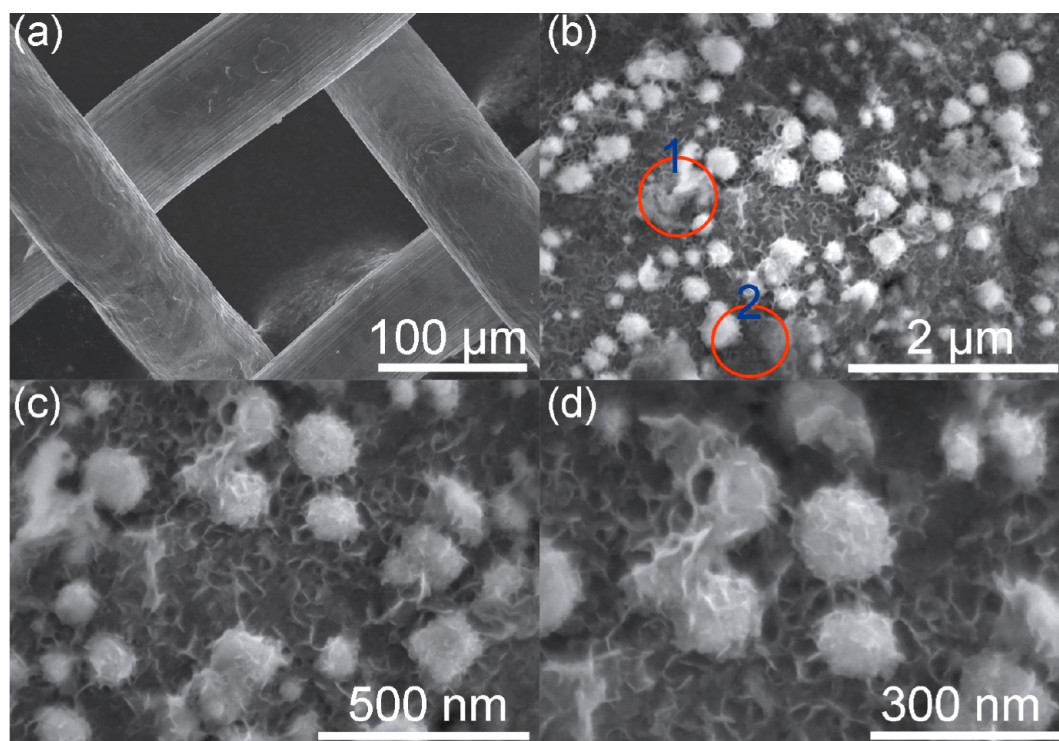


Figure 4. FESEM surface images of the samples supported by SS substrates: (a) 3D network architecture of SS; (b) RGO/Ni(OH)₂ films prepared at a voltage of 5 V and deposition time of 120 s, markers 1 and 2 reveal the presence of RGO; (c) RGO/Ni(OH)₂ flower-like morphology of the same sample in panel b; (d) high-magnification images of the RGO/Ni(OH)₂ flower-like structure and spherical flower-like nanoclusters of the same sample in panel b.

RGO/Ni(OH)₂ composites possess homogeneous microstructure although water decomposition is unavoidable under an applied potential of 10 V. It is significant that the morphologies of the materials are different with varying applied voltage. With increasing applied voltage, the applied field and the current density increase accordingly. Higher applied fields accelerate the deposition rate and influence the motion of the particles. Thus, the applied voltage affects the structure of the deposits.¹⁶ On the other hand, the process of water splitting can not be effectively inhibited, as mentioned above; when the applied voltage increases to 10 V, the gas bubbles also act on particle flux and movement, which may lead to different morphology of the deposits. In short, RGO/Ni(OH)₂ syntheses with homogeneous porous layered structure or sponge-like structure on NF substrates were prepared by controlled EPD of GO and Ni(NO₃)₂ hybrids dispersed in deionized water solution.

By changing NF substrate into SS substrate, we obtained different morphology of RGO/Ni(OH)₂ composites (the surface images of the samples deposited on ITO substrate, see Figure S3, and the morphologies of the samples deposited at different pH value are displayed in Figure S4). Figure 4a is a low-magnification FESEM image of the SS substrate. After the EPD process, RGO and Ni(OH)₂ deposit on SS substrate, illustrated by Figure 4b. There are lots of nanoparticle deposits on the surface of SS substrates. The selected areas of “1” and “2” marked by red circles indicate the presence of few RGO layers. The much higher magnitude FESEM image of Figure 4c shows that the syntheses have a flower-like morphology and some spherical nanoparticles with uniform needle-like petals locate on the surface of flower-like films. It is found that few layers of RGO present on the surface of flower-like film and

spherical nanoparticles. Since the thickness of single-layer RGO is only about 1 nm,³⁸ a higher magnitude FESEM image (see Figure 4d) is superior to discern the presence and the exact places of RGO. Yet in depositing the RGO and Ni(NO₃)₂ suspension, it has magically merged flower-like Ni(OH)₂ and few layers of RGO.

As discussed above, the EPD of materials deposited on SS substrates produces different morphologic structures compared with that on NF substrates. In spite of the similar variable tendency of deposition current curves, the intrinsic nature of substrates do play an important role in affecting the EPD process. The first factor is the conductivity of the substrates. It is known that low conductivity of the substrate leads to nonuniform film and slow deposition.³⁹ Moreover, it is compulsory to take some auxiliary tactic to realize the EPD process if the substrates are nonconducting materials.⁴⁰ The second factor is the microstructure of the substrate or its interaction with gas bubbles in aqueous suspension. Uchikoshi et al. compared four different EPD electrodes, i.e., Pt, Pd, Ni, and SS, to deposit Al₂O₃ from water and produced bubble-free deposits from an aqueous suspension as palladium absorbs hydrogen.⁴¹ Comparing with SS, the 3D porous structure of NF has the advantage of absorbing the gas bubbles, and hence it is less susceptible to water decomposition. The third factor is that the deposition rate is different using different substrates. By analyzing the deposition current of NF and SS (see Figure 2a and Figure S5), the current is higher for SS substrates than that for NF in the stable stage, as other EPD parameters are the same. The higher deposition rate causes more deposits at the same deposition time. We assume that the mutual effect of deposits on SS substrate is stronger than that on NF substrate, which yields flower-like films and partly agglomerated spherical

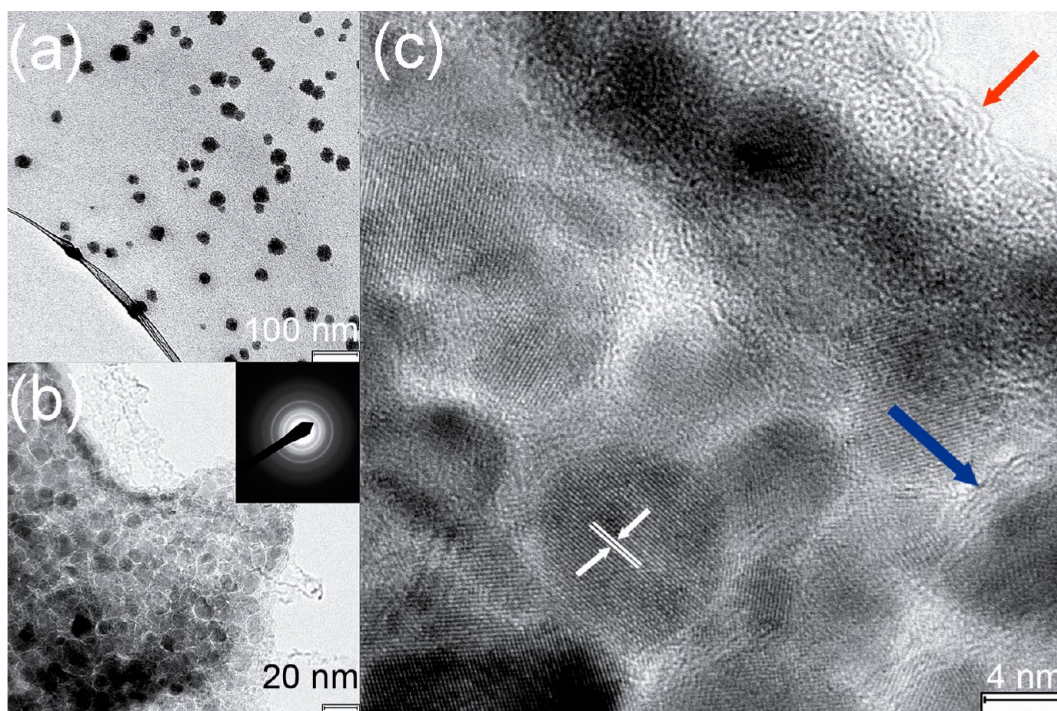


Figure 5. TEM images of GO/Ni(OH)₂ composite films: (a) low-magnification image of the samples, the dark approximately circular areas stand for Ni(OH)₂ nanoclusters, and the bright field is RGO; (b) typical morphology of Ni(OH)₂ nanoparticles anchored in layered RGO. The inset is the SAED of the sample; (c) high-magnification image of the sample; the red arrow indicates the edge of few-layer RGO.

Ni(OH)₂ nanoparticles. It was reported that nickel or cobalt hydroxide samples have incentive to form flower-like or porous structure by electrodeposition.^{42,43} The last factor is the stress between the substrate and the deposition film. The stress may not merely affect the morphology of deposition, but also it relates to the nucleation and crystallization, which we will discuss in the XRD part. In conclusion, by controlling other EPD factors the same way, we can obtain different morphologies of RGO/Ni(OH)₂ composite films using different conductive substrates.

Since few-layer RGO is only several nanometers and is functionalized by an oxygen functional group both in the basal plane and at the edge, we were motivated to figure out the interaction of nickel ions and GO, the transformation of nickel ions after the EPD process, the situation and the crystallization of Ni(OH)₂, and the morphology of RGO/Ni(OH)₂ composites. TEM characterization seems to be an effective method to help us understand these questions. Figure 5 shows TEM images of the selected sample named “C3-4”. The film was carefully stripped off from the Pt substrate and used for TEM characterization. As seen in Figure 5a, two apparent color differences exist: the bright areas and the dark areas. The bright areas represent the presence of RGO, while the dark areas represent the presence of Ni(OH)₂. Moreover, Ni(OH)₂ nanoclusters, which are made up of several Ni(OH)₂ nanoparticles, are well dispersed on the RGO, and the circular size of Ni(OH)₂ nanoclusters is approximately 20–50 nm. The high-magnification image (shown in Figure 5b) demonstrates that a dense layer of Ni(OH)₂ nanoparticles anchors on the RGO. Ni(OH)₂ nanoparticle is approximately circular, and the grain size is about 5–10 nm; the ultrafine grain size of Ni(OH)₂ may benefit from the protection of RGO.⁴⁴ Since RGO is a multilayer structure and almost every carbon atom layer will be decorated by the oxygen functional group during Hummer’s

method or some similar preparation method, it is reasonable to believe that nickel ions can incorporate into each layer of RGO. Thus, agglomeration-free multilayer RGO/Ni(OH)₂ composite films composed of RGO platelets and Ni(OH)₂ nanoclusters can be prepared by a one-step EPD process. The inset of Figure 5b is the SAED of the samples. On the basis of calibrating by Au (220) diffraction data using the external standard method, we confirmed that the three diffraction rings correspond to interplanar spacing of 2.61, 2.15, and 1.54 nm, respectively, which were quite consistent with the Miller indices (110)/(111), (103), (300) of α -Ni(OH)₂ (JCPDS No: 22-0444), indicating crystallization and polycrystalline of Ni(OH)₂ nanoparticles.

Figure 5c displays a high-magnification TEM image of the sample. One characterization is that the lattice phases have random orientation, demonstrating the polycrystalline nature of the sample, the same as the SAED result. Following the exact size of the indication notes by the white arrow, where interplanar spacing is 2.61 Å, (110) diffraction planes are identified. Another significant characterization noted by the red arrow is that bilayer RGO is observed. Furthermore, it can be seen that few-layer RGO, indicated by the blue arrow, is also present at ambient of crystallized Ni(OH)₂ nanoparticles. On the basis of FESEM, TEM, HRTEM, as well as SAED analysis, we draw a conclusion that nickel ions successfully anchor on layered RGO and transform into Ni(OH)₂ after the EPD process. The following characterization by XRD and XPS will further confirm that nickel ions transform into Ni(OH)₂. According to previous work, the 6-fold symmetry of the carbon atom planar would be destroyed experiencing a strong oxidation process, and the structure of GO was considered to be amorphous; the reestablishment of the symmetrical structure needs further chemical reducing action, known as the chemical reduced method, to produce graphene.⁴⁵ It implies that nickel

ions may play a role in reestablishing the symmetry of GO; a similar result regarding Fe reduction of GO was reported.⁴⁶ The third characterization is that Ni(OH)_2 nanoparticles are found to be present at both the inner planar and the edge of RGO, which means that both hydroxyl and carboxyl functionalized oxygen groups express mutual effect with nickel ions and induce the nucleation and the growth of Ni(OH)_2 .

Figure 6 shows the XRD patterns of RGO/Ni(OH)_2 composite films. For RGO/Ni(OH)_2 films on NF substrates,

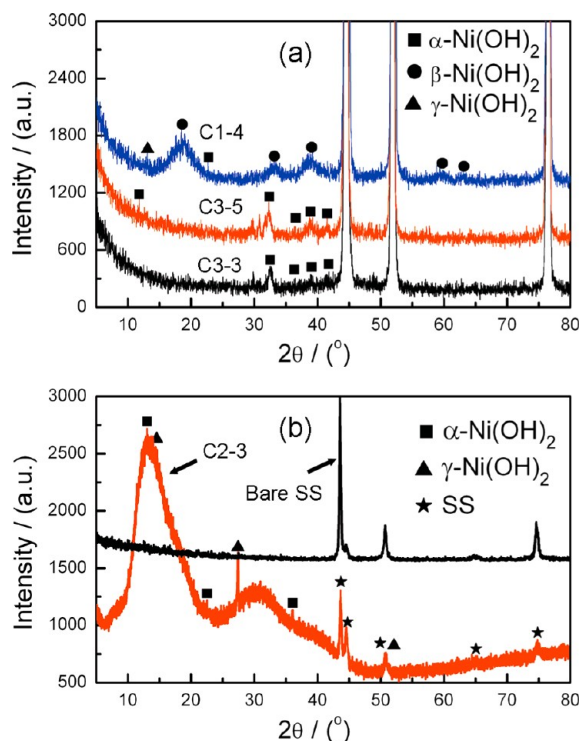


Figure 6. XRD patterns of RGO/Ni(OH)_2 composites film deposited on (a) NF and (b) SS substrates.

three selected samples named “C3-3”, “C3-5”, and “C1-4” were characterized, and the results are shown in Figure 6a. All the identified diffraction peaks appear in good agreement with standard powder diffraction patterns Ni(OH)_2 phase, indicating that most of the decorated nickel ions convert to Ni(OH)_2 after the EPD process. Because the codeposited nickel ions have small particle size with large surface area, it is reasonable that the oxidation of nickel ions may take place in EPD process, the same as electrochemical deposition of nickel salts. The broadness of the respective peaks of three samples contributes to nanorization of Ni(OH)_2 , and, as discussed in the TEM part, the grain size of Ni(OH)_2 nanoparticles is about 5–10 nm. Specifically, for the sample of “C1-4”, five diffraction peaks at around $2\theta = 17.5$ – 19.8 , 33.2 , 38.8 , 59.5 , and 62.9° correspond to the reflections from the (001), (100), (101), (110), and (111) planes of the β -phase (JCPDS No: 14-0117), respectively. One diffraction peak at around $2\theta = 12.84^\circ$ corresponds to the reflections from the (003) planes of γ -phase (JCPDS No: 06-0075), and one diffraction peak at around $2\theta = 22.78^\circ$ corresponds to the reflections from the (006) plane of α -phase (JCPDS No: 38-0715). In contrast with “C1-4”, the other two samples “C3-3” and “C3-5” prepared from stable colloidal suspensions possess a single phase of α -phase with diffraction peaks of (001) (the diffraction peak is not present in

“C3-3”), (110), (200), and (103) planes (JCPDS No: 22-0444). Additionally, three strong diffraction peaks originate from NF substrates, and the absence of the characteristic peak of RGO for the selected composite film may be due to the poor crystallinity of RGO.

Figure 6b shows the XRD pattern of the SS-supported RGO/Ni(OH)_2 syntheses. With the exclusion of four diffraction peaks from the SS substrate, another four diffraction peaks that belong to Ni(OH)_2 are observed. One strong and broad diffraction peak at around 10 – 15° represents the (001) plane of the α -phase (JCPDS No: 22-0444), the (003) plane of the γ -phase (JCPDS No: 06-0075), and not well-crystallized GO. The other two characteristic diffraction peaks with $2\theta = 23.9$ and 35.8° represent (002) and (111) planes of α -phase Ni(OH)_2 , while (006) and (108) planes of the γ -phase occur at $2\theta = 27.1$ and 51.3° . It can be inferred that the presence of GO and partly reduced GO may influence the crystallization of Ni(OH)_2 since a sharp broadness of the α -phase, the (003) plane of the γ -phase, and a broad amorphous diffraction background appears at around $2\theta = 30^\circ$. We assume that the functionalized oxygen can adsorb or probably chemically bond with nickel ions and consequently affect the nucleation, oxidation, and growth of nickel ions, but the exactly interaction mechanism needs further analysis and discussion. All in all, RGO/Ni(OH)_2 syntheses were prepared by the one-step EPD process, and the form of Ni(OH)_2 phase depended upon the colloidal suspension and the substrate.

We performed an XPS experiment on our RGO/Ni(OH)_2 composite films and compared it with GO powder. In order to avoid the influence of the nickel element from NF and SS substrates, we deposited RGO/Ni(OH)_2 samples on ITO substrate for XPS measurement. The C 1s XPS spectrum of GO (Figure 7a) clearly indicates a considerable degree of oxidation with four components that correspond to carbon atoms in different functional groups: the nonoxygenated ring C (284.4 eV), the C in C–OH bonds (285.6 eV), the epoxy C (286.5 eV), and C=O (288.0 eV). The presence of these peaks is in excellent agreement with previous work.⁴⁷ Compared to the GO spectrum, we find that RGO/Ni(OH)_2 has two recognizable peaks, assigned to the graphite carbon (284.8 eV) and a double-bonded carbon C=O peak (288.3 eV).⁴⁴ Although the C 1s XPS spectra of RGO/Ni(OH)_2 syntheses (Figure 7b) also exhibit broad oxygen functionality transition peaks that have been assigned for GO, the peak intensities of these components in the films are much smaller than those in GO powder, indicating considerable deoxygenation by the cathodic EPD process or possible nickel ions action. According to Shao et al.⁴⁸ and Wang et al.,⁴⁹ oxygen-functionalized GO was electrochemically reduced at the first cycle of extended cyclic voltammetry, and the reduction process was irreversible. Considering that positively charged GO reached the substrates under a negative electric potential, which would play a positive role in reducing GO to RGO. From semiquantitative analysis of XPS, the value of C:O, except from oxygen atoms of Ni(OH)_2 in the form of α -phase, (JCPDS No: 22-0444) based on our XRD and SAED characterizations is approximately 4.75:1, which is much higher than that in GO (about 2:1); while lower than that in chemically reduced GO, that value can reach up to 10:1.⁴² In addition, the binding energy of $\text{Ni } 2\text{P}_{3/2}$ and $\text{Ni } 2\text{P}_{1/2}$ (see Figure 7c) is 856.8 and 874.7 eV, respectively, associated with Ni(OH)_2 ,⁵⁰ which is consistent with our XRD and SAED characterizations.

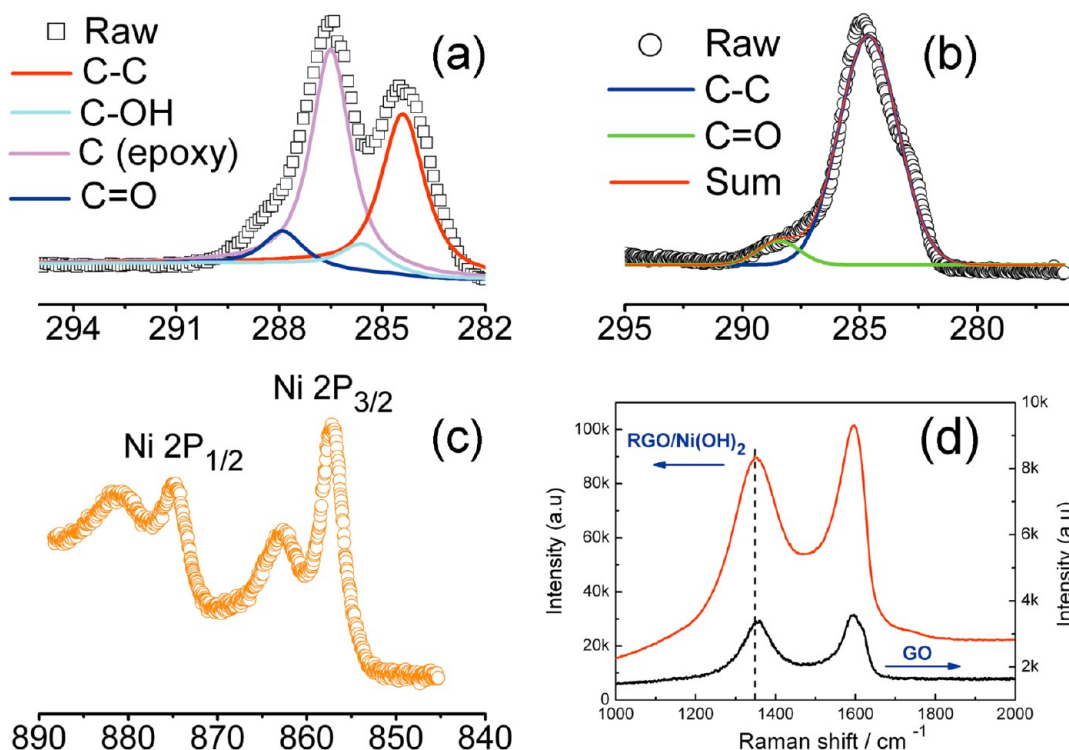


Figure 7. XPS and Raman spectra of the samples: (a) C 1s XPS of GO; (b) C 1s of RGO/Ni(OH)₂; (c) Ni 2p of RGO/Ni(OH)₂; (d) Raman spectra of GO and RGO/Ni(OH)₂.

On the basis of previous studies of the structure of GO and its chemical reactivity and on our own analytical data, one can speculate that the EPD process for deposition of GO and Ni(NO₃)₂ colloidal suspensions most likely yield partially reduced GO materials that are comprised of graphitic regions in addition to oxygen-functionalized carbon atoms.

RGO/Ni(OH)₂ composite has also been characterized by Raman spectroscopy (Figure 7d). The most important features in the Raman spectra obtained using a laser excitation of 514 nm are the G band appearing around 1580 cm⁻¹ and the disorder-induced D band at 1350 cm⁻¹, respectively.⁵¹ The Raman spectra in Figure 7d compare GO powder and RGO/Ni(OH)₂ composite films. The first-order G-mode appears in both samples at 1596 cm⁻¹, whereas in the D-mode for RGO/Ni(OH)₂ composite films, a clear shift in peak frequency from 1359 to 1348 cm⁻¹ is observed. This is similar to the data reported by Ganganahalli et al. for the electrochemical reduction of GO to RGO, where a difference of 10 cm⁻¹ is observed in the band positions before and after reduction.⁵² However, the nickel ions decoration and EPD process do not appear to have a negative influence on the material integrity. In fact, the I_D/I_G ratio, which is a measure of the defects in the carbon network, remains almost constant after the EPD process. From the analysis of Raman spectra data, we can conclude that the nickel ions decoration and EPD process are not detrimental to the sp² structure of graphite.

Self-assembly EPD of these composite films have been accomplished on conductives to create a multilayer or flower-like configuration of RGO/Ni(OH)₂ composites as a binder-free electrode for supercapacitor application. For this purpose, thin film electrodes deposited on NF were assembled in a three-electrode configuration, and the assembly was immersed in aqueous 6 M KOH solution for electrochemical measurements. The electrochemical performance of the GO and RGO/

Ni(OH)₂ was analyzed using CV and galvanostatic charge–discharge. The CV curves of the bare NF and RGO/Ni(OH)₂ device deposited on NF were measured with a scan rate at 50 mVs⁻¹. As shown in Figure 8a, CV curves display an apparent redox reaction peak, indicating that an efficient faradic capacitance is established in RGO/Ni(OH)₂ electrodes. The

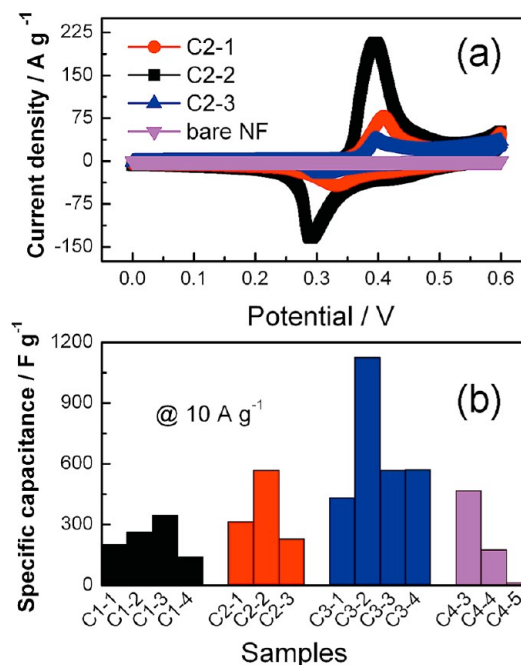


Figure 8. Electrochemical properties of EPD samples: (a) CV curves of the selected samples; (b) specific capacitance of the samples depends on discharge current density at 10 A g⁻¹.

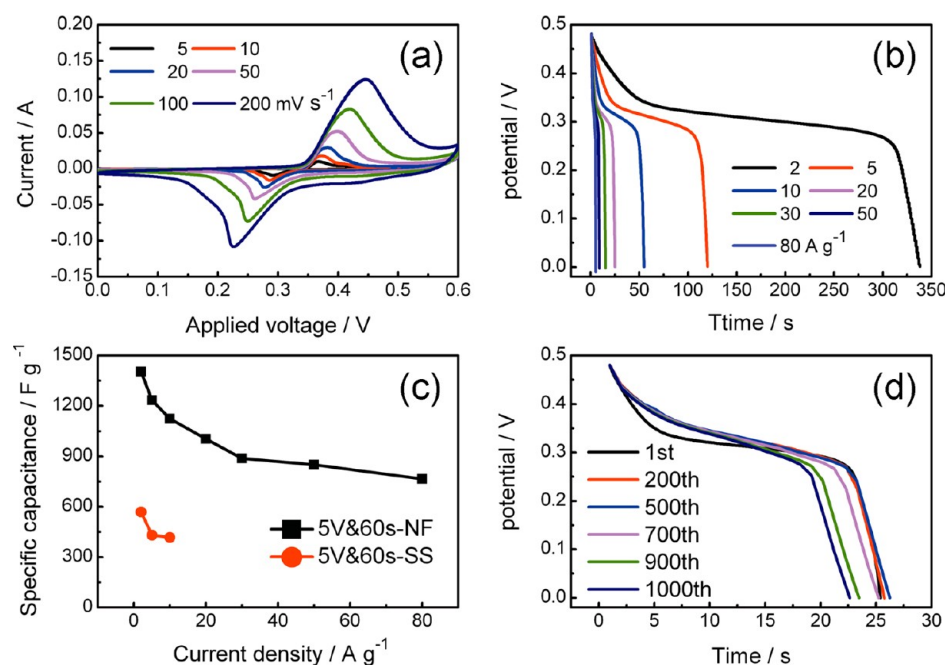


Figure 9. Electrochemical properties of the specific sample named “C3-2”: (a) CV curves with scanning rate ranges from 5 to 200 mV s^{-1} ; (b) the discharge curves of the samples at different specific current with a potential window of 0.48 V; (c) the specific capacitance versus the specific current calculated by the second discharge process; (d) cycling performance at 20 A g^{-1} .

redox couple at about 0.39 and 0.29 V is ascribed to the phase transition from $\alpha\text{-Ni}(\text{OH})_2$ to $\gamma\text{-Ni}(\text{OH})_2$ and vice versa, as represented by the electrochemical reaction given in eq 3.⁵³



One more remarkable difference of these CV curves is that the specific current of “C2-2” synthesized at EPD of 5 V is much higher than the samples prepared at EPD of 2 and 10 V. We think that the different structure and uniformity of the film induced by different applied potential give rise to the distinct electrochemical properties. As discussed earlier, the samples deposited at 5 V have multilayer structure, while the samples deposited at 10 V have the sponge-like structure. However, if applied potential is 2 V, the deposition weight is light, and the uniformity of the film is inferior, which lead to inferior performance of the samples. In addition, since the contribution to the electrochemical performance of bare NF is rather low, the effect of the substrates can be neglected.

The specific capacitance for the samples was obtained at a discharge current density of 10 A g^{-1} calculated from galvanostatic charge–discharge curves (Figure 8b); the measured mass for each electrode in GO and RGO/ $\text{Ni}(\text{OH})_2$ device is summarized in Table 2. Disordered-structure and poor-conductivity lead to low specific capacitance of GO (the detailed electrochemical performances of GO was given in Figure S6). After decorating by Ni ions and experiencing the EPD process, the RGO/ $\text{Ni}(\text{OH})_2$ composite films can be produced and their electrochemical properties are significantly dependent on the condition of the EPD process. In general, suitable applied potential, stable colloidal suspension, higher concentration of $\text{Ni}(\text{NO}_3)_2$, and appropriate deposition time are key parameters to high-quality film and high electrochemical performance. Therefore, the samples prepared at 5 V reveal higher specific capacitance than that at 2 and 10 V. Compared with preparing from stale colloidal suspensions as adding the weight of $\text{Ni}(\text{NO}_3)_2$ from 5 to 20 mg, the sample

prepared from unstable solution with the concentration of 0.5 mmol $\text{Ni}(\text{NO}_3)_2$ and 0.4 g L^{-1} GO aqueous solution shows rather low specific capacitance, that is, 138 F g^{-1} at 10 A g^{-1} . When the concentration of $\text{Ni}(\text{NO}_3)_2$ and the applied potential were fixed, we find that the deposition time of 60 s is more suitable than other deposition times like 30 s, 120 s, or even longer. The highest specific capacitance of “C3-2” is 1125 F g^{-1} at 10 A g^{-1} based on the mass of RGO and $\text{Ni}(\text{OH})_2$. The reasons may ascribe to the uniformity and the layered structure of deposited films, as discussed above. However, the electrochemical performances of “C4-3” and “C4-4” are inferior when KOH is added to adjust the pH value of the deposition solution. This may be attributed to the different morphology compared with “C3-2” (see Figure S4). The extremely low specific capacitance of “C4-5” prepared by the anodic EPD process is ascribed to its pure GO structure.

After optimizing EPD parameters, the sample named “C3-2” possesses excellent electrochemical performance, thus, we will further discuss here, and the results are shown in Figure 9. The CV curves with a scanning rate from 5 to 200 mV s^{-1} are revealed in Figure 9a. One strong oxidation peak is attributed to the transition from $\alpha\text{-Ni}(\text{OH})_2$ to $\gamma\text{-Ni}(\text{OH})_2$; such peaks are related to Faradaic reactions of $\text{Ni}(\text{OH})_2$ described by the well-accepted reaction of eq 3. The linear increment of oxidation peak with increasing the scanning rate from 5 to 200 mV s^{-1} indicates a diffusion mechanism of hydroxyl ions. There is an additional redox peak when the scanning rate decreases to 20 mV s^{-1} or even lower. It is known that the anodic peak of $\beta\text{-Ni}(\text{OH})_2$ has a higher potential with respect to that of $\alpha\text{-Ni}(\text{OH})_2$ in the anodic direction.⁵⁴ It is possible that the appearance of the new peak indicates the formation of $\beta\text{-Ni}(\text{OH})_2$. However, the oxidation peak is absent when the scanning rate is higher than 20 mV s^{-1} , which implies that the reaction rate of $\beta\text{-Ni}(\text{OH})_2$ is lower than that of $\alpha\text{-Ni}(\text{OH})_2$.

For these materials to be suitable for use in electrochemical capacitors, they should exhibit the characteristic of maintaining

high utilization at high currents. Hence, galvanostatic charge–discharge experiments were conducted on the RGO/Ni(OH)₂ composites film to qualify the loss in capacity at high discharge rates. Figure 9b shows the discharge curves under a potential window of 0.48 V for the sample with discharge current density ranging from 2 to 80 A g^{−1}. The corresponding specific capacitance is 1404 F g^{−1} and retains 1004 F g^{−1} at 20 A g^{−1}; even at 80 A g^{−1}, the value retains 767 F g^{−1} based on the total mass of Ni(OH)₂ and RGO (shown in Figure 9c). The specific capacitance at 2 A g^{−1} is high due to the low ohmic drop and inner active sites of the electrode being fully accessible. The low specific capacitance at higher scan rates compared to lower scan rates is mainly due to the increase in ionic resistivity and the inaccessibility of the electrode surface at high charge–discharge rates.⁵⁵ Remarkably, the prominently electrochemical performances of RGO/Ni(OH)₂ are comparable with that of graphene/Ni(OH)₂ in which the specific capacitance is 935 F g^{−1} at 2.8 A g^{−1}, 1026 F g^{−1} at 5.7 A g^{−1}, and 1215 F g^{−1} at 5 mV s^{−1} based on the mass of graphene and Ni(OH)₂.^{56–58} Several factors promote the superior electrochemical performances of the materials. First, the synergistic effect of RGO and Ni(OH)₂ particles yield aggregation-free multilayer RGO/Ni(OH)₂ syntheses, which enables an effective redox reaction at the interface of Ni(OH)₂ particles and electrolyte. Second, many oxygen functional groups of GO act as anchor sites for Ni(OH)₂ particles and can be synthesized in situ at the basal planes and edges of RGO. Moreover, the grain size Ni(OH)₂ is only 5–10 nm, which provides higher electrode/electrolyte contact area, shortens path lengths for electronic transport and ion transport, and thus Ni(OH)₂ nanoparticles possess high capacity and ultrafast energy storage capability.⁵⁹ In addition, the 3D porous structure of NF provides larger specific area and can significantly reduce the diffusion length of ions. Importantly, the low resistance of RGO/Ni(OH)₂ and the contact resistance between RGO/Ni(OH)₂ and current collector NF will enhance the rate that the supercapacitor can be charged and discharged.⁶⁰ For comparison, Figure 9c also shows that the specific capacitance (572 F g^{−1} at 2 A g^{−1}) of mixed α - and γ -Ni(OH)₂/RGO deposited on SS substrates is rather low relative to that on NF substrates, which probably results from the different crystal structure, partial agglomerate morphology, and weakly cohesive force between spherical nanoparticles and flower-like Ni(OH)₂ films.

Another significantly related performance of pseudocapacitors is cycling lifetime. The RGO/Ni(OH)₂ pseudocapacitors also exhibits good cycling stability (Figure 9d) with a stable capacitance (~89.8% of the original capacitance) after 1000 cycles of charging and discharging at a current density of 20 A g^{−1}. That cyclic stability is superior to that in pure Ni(OH)₂ materials, in which the specific capacitance decreases by as much as 20–50% after 300–1000 cycling.^{61–63} The stable cycling performance is related to the multilayer porous structure of the samples, the synergistic effect of RGO, and the increased effective interfacial area between Ni(OH)₂ and electrolyte. Indeed, the integrated multilayer films of RGO/Ni(OH)₂ provides a shortened diffusion path for both electrons and ions, improves the charge–discharge efficiency, and restrains the strain during ion intercalation. Moreover, multilayer porous structure of RGO/Ni(OH)₂ syntheses holds the advantage that it can relax the tension caused by the volume change induced by phase transformation of Ni(OH)₂,⁵⁷ resulting in better cycling performance. Electrochemical stability of polyaniline electrode materials was greatly

improved after incorporating graphene/GO.^{35–37} The key to the stability effect of RGO for Ni(OH)₂ nanoparticle in situ growth and intercalation is that RGO encapsulates the Ni(OH)₂ and allows for electrochemical Ni(OH)₂/NiOOH redox switching, which is critical to high cyclic stability.

CONCLUSIONS

A method for performing EPD on several conducting substrates has been developed to produce RGO/Ni(OH)₂ composite films. Self-assembly one-step EPD, where the process of water decomposition was effectively inhibited, was carried out in aqueous solution at a low applied voltage of 2–10 V. The success of one-step EPD of RGO/Ni(OH)₂ is significant as it enables simple, scalable, low-cost, and environmentally friendly deposition. The multilayer structure of α -Ni(OH)₂/RGO deposited on NF substrates and the flower-like structure of coexisting α -Ni(OH)₂/RGO with γ -Ni(OH)₂/RGO deposited on SS substrates have been synthesized by controlling the parameters of EPD. Ni(OH)₂ nanocrystals by in situ transformation from nickel ions had a uniformly distributed grain size of 5–10 nm and anchored on RGO. RGO/Ni(OH)₂ syntheses possessed advanced pseudocapacitance performances because of the synergetic effect of the two nanomaterials.

ASSOCIATED CONTENT

Supporting Information

EPD current curves; EDS of the samples; FESEM of GO and GO/Ni(OH)₂ on ITO substrate; FESEM of GO/Ni(OH)₂ deposited at different pH values; electrochemical properties of GO. This material is available free of charge via the Internet at <http://pubs.acs.org>.

AUTHOR INFORMATION

Corresponding Author

*Tel.: +86 10 82547129. Fax: +86 10 82547137. E-mail: ywma@mail.iese.ac.cn.

Author Contributions

The manuscript was written through contributions of all authors. All authors have given approval to the final version of the manuscript.

Notes

The authors declare no competing financial interest.

ACKNOWLEDGMENTS

This work was supported by the Knowledge Innovation Program of the Chinese Academy of Sciences (No. KJCX2-YW-W26), the Beijing Municipal Science and Technology Commission (No. Z111100056011007), and the National Natural Science Foundation of China (Nos. 21001103 and 51025726). The authors would like to acknowledge Xifeng Zhang for the FESEM and Jie Sun for ζ -potential measurements. We acknowledge the use of TEM facilities at the Institute of Physics, Chinese Academy of Sciences.

REFERENCES

- (1) Koz, R.; Carlen, M. *Electrochim. Acta* **2000**, *45*, 2483–2498.
- (2) Ribeiro, P. F.; Johnson, B. K.; Crow, M. L.; Arsoy, A.; Liu, Y. *Proc. IEEE* **2001**, *89*, 1744–1756.
- (3) Simon, P.; Gogotsi, Y. *Nat. Mater.* **2008**, *7*, 845–854.
- (4) Subramanian, V.; Zhu, H.; Vajtai, R.; Ajayan, P. M.; Wei, B. J. *Phys. Chem. B* **2005**, *109*, 20207–20214.
- (5) Andrieu, X. *Electron.: New Trends Electrochem. Technol.* **2000**, *1*, 521–547.

- (6) Frackowiak, E.; Béguin, F. *Carbon* **2001**, 39, 937–950.
- (7) Jang, J. H.; Kato, A.; Machida, K.; Naoi, K. *J. Electrochem. Soc.* **2006**, 153, A321–A328.
- (8) Lang, X.; Hirata, A.; Fujita, T.; Chen, M. *Nat. Nanotechnol.* **2011**, 6, 232–236.
- (9) Yang, G.-W.; Xu, C.-L.; Li, H.-L. *Chem. Commun.* **2008**, 6537–6539.
- (10) Gupta, V.; Gupta, S.; Miura, N. *J. Power Sources* **2008**, 175, 680–685.
- (11) Conway, B.; Birss, V.; Wojtowicz, J. *J. Power Sources* **1997**, 66, 1–14.
- (12) Wang, G.; Zhang, L.; Zhang, J. *Chem. Soc. Rev.* **2012**, 41, 797–828.
- (13) Van der Biest, O. O.; Vandeperre, L. *J. Annu. Rev. Mater. Sci.* **1999**, 29, 327–352.
- (14) Fukada, Y.; Nagarajan, N.; Mekky, W.; Bao, Y.; Kim, H. S.; Nicholson, P. S. *J. Mater. Sci.* **2004**, 39, 787–801.
- (15) Corni, I.; Ryan, M. P.; Boccacini, A. R. *J. Eur. Ceram. Soc.* **2008**, 28, 1353–1367.
- (16) Besra, L.; Liu, M. *Prog. Mater. Sci.* **2007**, 52, 1–61.
- (17) Wu, Z.-S.; Pei, S.; Ren, W.; Tang, D.; Gao, L.; Liu, B.; Li, F.; Liu, C.; Cheng, H.-M. *Adv. Mater.* **2009**, 21, 1756–1760.
- (18) Chen, Y.; Zhang, X.; Yu, P.; Ma, Y. *J. Power Sources* **2010**, 195, 3031–3035.
- (19) Chen, Y.; Zhang, X.; Yu, P.; Ma, Y. *Chem. Commun.* **2009**, 4527–4529.
- (20) An, S. J.; Zhu, Y.; Lee, S. H.; Stoller, M. D.; Emilsson, T.; Park, S.; Velamakanni, A.; An, J.; Ruoff, R. S. *J. Phys. Chem. Lett.* **2010**, 1, 1259–1263.
- (21) Seger, B.; Kamat, P. V. *J. Phys. Chem. C* **2009**, 113, 7990–7995.
- (22) Lu, T.; Pan, L.; Li, H.; Nie, C.; Zhu, M.; Sun, Z. *J. Electroanal. Chem.* **2011**, 661, 270–273.
- (23) Xia, X.; Tu, J.; Mai, Y.; Chen, R.; Wang, X.; Gu, C.; Zhao, X. *Chem.—Eur. J.* **2011**, 17, 10898–10905.
- (24) Wu, M.-S.; Lin, Y.-P.; Lin, C.-H.; Lee, J.-T. *J. Mater. Chem.* **2012**, 22, 2442–2448.
- (25) Mini, P. A.; Balakrishnan, A.; Nair, S. V.; Subramanian, K. R. *Chem. Commun.* **2011**, 47, 5753–5755.
- (26) Hayashi, H.; Lightcap, I. V.; Tsujimoto, M.; Takano, M.; Umeyama, T.; Kamat, P. V.; Imahori, H. *J. Am. Chem. Soc.* **2011**, 133, 7684–7687.
- (27) Besra, L.; Compson, C.; Liu, M. *J. Am. Ceram. Soc.* **2006**, 89, 3003–3009.
- (28) Grillon, F.; Fayeulle, D.; Jeandin, M. *J. Mater. Sci. Lett.* **1992**, 11, 272–275.
- (29) Trau, M.; Saville, D. A.; Aksay, I. A. *Science* **1996**, 272, 706–709.
- (30) Hamaker, H. C. *Trans. Faraday Soc.* **1940**, 35, 279–287.
- (31) An, K. H.; Kim, W. S.; Park, Y. S.; Moon, J. M.; Bae, D. J.; Lim, S. C.; Lee, Y. S.; Lee, Y. H. *Adv. Func. Mater.* **2001**, 11, 387–392.
- (32) Wu, M.-S.; Lin, K.-H. *J. Phys. Chem. C* **2010**, 114, 6190–6196.
- (33) Lerf, A.; He, H.; Forster, M.; Klinowski, J. *J. Phys. Chem. B* **1998**, 102, 4477–4482.
- (34) Dreyer, D. R.; Park, S.; Bielawski, C. W.; Ruoff, R. S. *Chem. Soc. Rev.* **2010**, 39, 228–240.
- (35) Xu, J.; Wang, K.; Zu, S.-Z.; Han, B.-H.; Wei, Z. *ACS Nano* **2010**, 4, 5019–5026.
- (36) Wu, Q.; Xu, Y.; Yao, Z.; Liu, A.; Shi, G. *ACS Nano* **2010**, 4, 1963–1970.
- (37) Zhang, K.; Zhang, L. L.; Zhao, X. S.; Wu, J. *Chem. Mater.* **2010**, 22, 1392–1401.
- (38) Stankovich, S.; Dikin, D. A.; Piner, R. D.; Kohlhaas, K. A.; Kleinhammes, A.; Jia, Y.; Wu, Y.; Nguyen, S. T.; Ruoff, R. S. *Carbon* **2007**, 45, 1558–1565.
- (39) Chen, F.; Liu, M. *J. Eur. Ceram. Soc.* **2001**, 21, 127–134.
- (40) Peng, Z.; Liu, M. *J. Am. Ceram. Soc.* **2001**, 84, 283–288.
- (41) Uchikoshi, T.; Ozawa, K.; Hatton, B. D.; Sakka, Y. *J. Mater. Res.* **2001**, 16, 321–324.
- (42) Pan, G. X.; Xia, X.; Cao, F.; Tang, P. S.; Chen, H. F. *Electrochim. Acta* **2012**, 63, 335–340.
- (43) Lu, Z.; Chang, Z.; Zhu, W.; Sun, X. *Chem. Commun.* **2011**, 47, 9651–9653.
- (44) Cassagneau, T.; Fendler, J. H. *J. Phys. Chem. B* **1999**, 103, 1789–1793.
- (45) Park, S.; Ruoff, R. S. *Nat. Nanotechnol.* **2009**, 4, 217–224.
- (46) Fan, Z.-J.; Kai, W.; Yan, J.; Wei, T.; Zhi, L.-J.; Feng, J.; Ren, Y.-m.; Song, L.-P.; Wei, F. *ACS Nano* **2011**, 5, 191–198.
- (47) Yang, D.; Velamakanni, A.; Bozoklu, G.; Park, S.; Stoller, M.; Piner, R. D.; Stankovich, S.; Jung, I.; Field, D. A.; Ventrice, C. A., Jr; et al. *Carbon* **2009**, 47, 145–152.
- (48) Wang, Z.; Zhou, X.; Zhang, J.; Boey, F.; Zhang, H. *J. Phys. Chem. C* **2009**, 113, 14071–14075.
- (49) Shao, Y.; Wang, J.; Engelhard, M.; Wang, C.; Lin, Y. *J. Mater. Chem.* **2010**, 20, 743–748.
- (50) Wagner, C. D.; Riggs, W. M.; Davis, L. E.; Moulder, J. F.; Muilenberg, G. E. *Handbook of X-ray Photoelectron Spectroscopy: A Reference Book of Standard Data for Use in X-ray Photoelectron Spectroscopy*; Perkin-Elmer: Eden Prairie, MN, 1979.
- (51) Ferrari, A. C.; Meyer, J. C.; Scardaci, V.; Casiraghi, C.; Lazzeri, M.; Mauri, F.; Piscanec, S.; Jiang, D.; Novoselov, K. S.; Roth, S.; et al. *Phys. Rev. Lett.* **2006**, 97, 187401.
- (52) Ramesha, G. K.; Sampath, S. *J. Phys. Chem. C* **2009**, 113, 7985–7989.
- (53) Fleischmann, M.; Korinek, K.; Pletcher, D. *J. Electroanal. Chem., Interfacial Electrochem.* **1971**, 31, 39–49.
- (54) Sac-Epee, N.; Palacin, M. R.; Delahaye-Vidal, A.; Chabre, Y.; Tarascon, J. M. *J. Electrochem. Soc.* **1998**, 145, 1434–1441.
- (55) Yuan, C.-Z.; Gao, B.; Zhang, X.-G. *J. Power Sources* **2007**, 173, 606–612.
- (56) Wang, H.; Casalongue, H. S.; Liang, Y.; Dai, H. *J. Am. Chem. Soc.* **2010**, 132, 7472–7477.
- (57) Lee, J. W.; Ahn, T.; Soundararajan, D.; Ko, J. M.; Kim, J.-D. *Chem. Commun.* **2011**, 47, 6305–6307.
- (58) Yang, S.; Wu, X.; Chen, C.; Dong, H.; Hu, W.; Wang, X. *Chem. Commun.* **2012**, 48, 2773–2775.
- (59) Arico, A. S.; Bruce, P.; Scrosati, B.; Tarascon, J.-M.; van Schalkwijk, W. *Nat. Mater.* **2005**, 4, 366–377.
- (60) Burke, A. *J. Power Sources* **2000**, 91, 37–50.
- (61) Yang, G.-W.; Xu, C.-L.; Li, H.-L. *Chem. Commun.* **2008**, 6537–6539.
- (62) Hu, G.; Li, C.; Gong, H. *J. Power Sources* **2010**, 195, 6977–6981.
- (63) Yuan, Y.-F.; Xia, X.-H.; Wu, J.-B.; Yang, J.-L.; Chen, Y.-B.; Guo, S.-Y. *Electrochim. Acta* **2011**, 56, 2627–2632.